Journal of Luminescence 206 (2019) 442–454

Contents lists available at ScienceDirect

Journal of Luminescence

journal homepage: www.elsevier.com/locate/jlumin

Luminescence properties of α-Ag_2WO_4 nanorods co-doped with Li^+ and Eu^{3+} cations and their effects on its structure

Ivo M. Pinatti[a,b], George R. Fern[a], Elson Longo[b], Terry G. Ireland[a,*], Paula F.S. Pereira[b], Ieda L.V. Rosa[b], Jack Silver[a]

[a] Wolfson Centre for Materials Processing, Brunel University London, Kingston Lane, Uxbridge, Middlesex UB8 3PH, UK
[b] INCTMN, LIEC, Chemistry Department of the Federal University of São Carlos, P.O. Box 676, 13565-905 São Carlos, SP, Brazil

ARTICLE INFO

Keywords:
Red phosphors
LEDs
Ag_2WO_4 lattice
Eu^{3+} activation
Li^+ co activator

ABSTRACT

Nanorods of the formula α-$(Ag_{2-3\times y}Eu_xLi_y)WO_4$ (where x = 0.01, y = 0.01–0.03 mol) were efficiently synthesized via a low temperature (90 °C) co-precipitation (CP) method. They were structurally characterised using both: X-ray powder diffraction (Rietveld refinement) and low temperature (20 °C to −190 °C) micro-Raman spectroscopy. The morphology of the nanorods was confirmed with field emission scanning electron microscopy. The peaks in the XRD patterns of α-$(Ag_{2-3\times y}Eu_xLi_y)WO_4$ samples were all indexed to the pure orthorhombic phase of α-Ag_2WO_4 and are in good accordance with ICSD n° 4165. These results indicate that Eu^{3+} and Li^+ ions have both been introduced efficiently into the α-Ag_2WO_4 lattice. Moreover, the Li^+ co-dopant facilitated smoother incorporation of Eu^{3+} concentration into the α-Ag_2WO_4 lattice with less distortion of the lattice. In addition the presence of the Li^+ co-dopant eases strain in the lattice and this allows the incorporated Eu^{3+} cations to emit red light much more efficiently. This is seen for α-$(Ag_{2-3\times y}Eu_xLi_y)WO_4$ (where x = 0.01, y = 0.02 mol) in which the optimum red emission is observed. Analysis of the emission spectra in respect to the known metal coordination sites in the structure suggest the Eu^{3+} cations are only in Ag1 and Ag2 sites which are coordinated by seven O atoms (AgO_7 deltahedral polyhedrons). This finding is also confirmed by the photoluminescent decay curves which can be analysed in terms of one depopulation mechanism is in accord with the occurrence of a single coordination environment for the Eu^{3+} cations. Although the co-doped α-$(Ag_{2-3\times y}Eu_xLi_y)WO_4$ phosphors are much brighter than those containing no Li^+ cations they are not bright enough (as yet) to be used in commercial devices.

1. Introduction

We have previously discussed four different ways of producing white light from blue light emitting diodes (LEDs). However if good colour rendering is required then the best method is to use both green and red emitting conversion phosphors in combination with a blue LED [1].

Over the last fifteen or so years a large number of Eu^{3+}-doped tungstate based lattices have been reported for possible application as red conversion phosphors. Previously [2] we listed a range of examples of such papers [3–17]. The resulting Eu^{3+} activated phosphor lattices all manifest intense narrow red emission bands which when added to a blue LED and an additional green emitting phosphor would generate a "white spectrum" which of cause is not the optimum way of making a good white. In addition some of these materials require high amounts of the expensive europium activator. Obviously, due to the price and scarcity of the later rare earth element, it would be better to reduce the amount present.

The metal tungstate lattices have been chosen as possible hosts for red emitting phosphors when doped with Eu^{3+} as they are semiconductor materials manifesting wide band-gaps. They are in many cases self-activating phosphors, Amongst, the many attributes inherent to such tungstate lattices, are their low toxicities, high chemical stabilities, good X-ray absorption coefficients and useful light yields [18]. Moreover, tungstate host lattices manifest low phonon energy which will minimize the losses due to non-radiative transitions resulting in increased quantum efficiency.

In the case of M^{3+} cations (where M^{3+} is a rare earth element), they manifest spectra that arise from f-f transitions. Electrons in these f orbitals are shielded from their surroundings and are relatively unaffected by external bonding though they are sensitive to the symmetry of the bonding. This shielding makes the emission and excitation bands very

* Corresponding author.
E-mail address: terry.ireland@brunel.ac.uk (T.G. Ireland).

https://doi.org/10.1016/j.jlumin.2018.10.104
Received 2 May 2018; Received in revised form 19 October 2018; Accepted 23 October 2018
Available online 26 October 2018

narrow. Eu^{3+} cations manifest a large energy gap between the lowest luminescent energy state and the highest non-luminescent energy state that gives rise to strong luminescence intensity. This is why Eu^{3+} cations require host lattices such as the metal tungstates that have wide band gaps that will not interfere with their emission. As the emission bands arising from Eu^{3+} activated phosphors are very dependent on the symmetry of the emission sites in the host lattices then they depend strongly on the symmetry of the crystal structure of the lattice as well as its uniformity. Hence the nature of and number of different doping sites in the lattice in addition to the doping concentration of the activator that is emitting will all be important to the overall photoluminescence emission properties and must be understood. For the doping sites present in the host lattice, factors such as distance between dopants, the coordination number of each site and its symmetry as well as its relative spatial position and its electronic environment will need to be considered [19]. So as discussed above Eu^{3+} activated tungstate lattices have been shown to manifest excellent luminescent efficiency and colour purity in addition to having high average refractive indexes [3–17]. In addition to their already mentioned advantages they can often be synthesized at low temperatures [2]. Finally they also manifest broad intense ligand-to-metal charge transfer (LMCT) band(s) in the UV or near-UV region that are ideal to couple to the emission from an InGaN-based LED.

The possible application of these compounds as red phosphors for use with blue emitting LEDs and a green or yellow phosphor to produce a white light (pc-WLEDs, phosphor-converted LEDs) is appealing to the lighting industry to further the use of GaN or InGaN chips particularly for backlight applications in display devices [20]. The majority of the current pc-WLEDs in the market place have poor colour rendering indexes (CRI) due to the lack of a suitable red component for white light emission and though there are a number of red phosphors in the latest pc-WLEDs this still remains a long-standing open challenge. Solid state lighting using inorganic compounds doped with rare earth cations now dominates the lighting market; it is of course very much more appealing than traditional lighting (incandescent and fluorescent lamps) because of its low energy consumption, longer lifetime, high reliability, higher energy efficiency and it has more friendly environment implications [21,22]. Spin off uses of LED phosphors are in the astrophysics area are being explored [23] as well as in some X-ray detector systems [24]. Other uses include enhanced photoelectric conversion efficiency for use in dye sensitized solar cells; [25] Eu^{3+}-doped $GdVO_4$ nanocrystals have been reported as a luminescent probe for hydrogen peroxide and for enzymatic sensing of glucose [26].

In this work we will report on a range of new red emitting Eu^{3+} doped tungstate phosphors and it is therefore useful to consider here the properties of these activator cations. Eu^{3+} ([Xe] $4f^6$) cations have optical properties that present several advantages compared to other rare earth elements besides their pure red emission. These relate to its use as a photoluminescence (PL) probe and include: ^5D_J (J = 0–3) levels that are well separated from $^5F_{J"}$ (J" = 0–6) levels; the emitting $^5D_0$ level and the ground state $^7F_0$ are nondegenerate; hence emission from the $^5D_0$ level to the ground state $^7F_0$ is allowed (by forced electric dipole) when the ion is in a lower symmetry site; magnetic dipole $^5D_0 \rightarrow {}^7F_1$ transition is allowed and labelled as a reference transition; the hypersensitive transition $^5D_0 \rightarrow {}^7F_2$ can give information about the covalent character of the rare-earth atom to ligand bond; the luminescence decay time of the emitting $^5D_0$ level is longer (ms) and it manifests a large Stokes' shift when directly excited in level $^5L_6$ (~394 nm) [27].

In the case of Eu^{3+} doped luminescent materials, emission colours can be further enhanced and tuned by introducing non-RE^{3+} ions as co dopants; exploring new (different) host lattices, experimental conditions, particle size, crystallinity and phase of the host material. Such approaches have been proved to be efficient and convenient methods both in down-conversion (DC) and up-conversion (UC) materials [28].

Herein we report further studies (see ref. 2) on Eu^{3+} doped α-Ag_2WO_4. The parent lattice α-Ag_2WO_4 is orthorhombic (space group *Pn2n)* [29]. As we have previously discussed [2] in this structure each W atom is bonded to six oxygen atoms and the Ag^+ cations are found to have two, four, six and seven-coordinated geometry. Both the WO_6 and AgO_6 clusters have site symmetry of O_h whereas the AgO_2, AgO_4 and AgO_7 polyhedra have lower symmetry. The Ag^+ cations are found in four different coordination sites; 15% of these sites are non-centro-symmetric with C_{2v} symmetry (AgO_2), 37% are non-centro-symmetric with T_d symmetry (AgO_4), 18% are centro-symmetric with O_h symmetry (AgO_6) and 30% are non-centro-symmetric with D_{5h} symmetry (AgO_7) [29–31]. It therefore follows that the electric dipole $^5D_0 \rightarrow {}^7F_2$ transition in the reported spectra is caused specifically by the Eu^{3+} located at one or more of the non-centro symmetric sites [32]. Due to the presence of so many sites with different coordination geometries that could possibly be available for dopant atoms, it is important to know the localization of rare earth ions in this material as doping each site is likely to produce different structural modifications in the matrix which may in turn modify the light emitting properties of the doping cations.

Silver tungstate (which has a band gap in the range of 2.9–3.4 eV) has many uses and has been suggested for many more [33–49]. Notable among these uses is in catalysis of organic compounds [34] and as antimicrobial and antibacterial agents [47–49]. A study of the influence of electron beam irradiation on both the structural and the optical properties of silver tungstate has also been reported [50].

Alkali-metal ions (Li^+, Na^+, and K^+) can be used as a co-dopants with Eu^{3+} in a phosphor lattice, and there are papers in the literature that show that these smaller cations can act as charge compensators and/or as sensitizers changing the CT band of the host lattice (O^{2-} - W^{6+}), enhancing the intensity of Eu^{3+} red emission and improving the colour purity of the material [51,52]. So it was thought (and is reported herein) that the addition of one of these cations may reduce the amount of Eu^{3+} needed to produce better and more efficient phosphors. Trivalent ions substituting monovalent cations can produce defects like vacancies or interstitial atom defects which can interfere with the absorbance of the energy from the excitation light and then decrease the luminescent intensity. To overcome such drawbacks it has been shown that the alkali metal ion Li^+ could be co-doped into α-Ag_2WO_4 to balance the charge and increase the luminescence [53].

Phosphors were traditionally manufactured industrially by solid state synthesis, as the method is scalable and requires less space. However this methodology has disadvantages as we have previously discussed [2,32]. We also discussed the merits of the co-precipitation route which is now widely used as an effective and environmentally benign method to prepare nanoscale shape-controlled material. Amongst the other advantages of the method is that it facilitates homogeneous atomic mixing of the phosphor precursors and yields precipitates with controlled uniform stoichiometry. The route is simple, versatile, and cost-effective yielding crystalline, chemically purified, single phase particles at lower temperatures, and it may facilitate overall shorter reaction times when compared to conventional solid-state reactions [54]. It is also a cheap chemical precipitation method that does not require a catalyst or capping agent [55]. The method often only requires simple equipment and short reaction times [56].

We previously reported that the red emitting Eu^{3+} doped silver tungstate α-$(Ag_{2-3x}Eu_x)WO_4$ (x = 0.0–0.01 mol) phosphor crystalizes as nanorods and it was suggested that it could be used for blue LED colour conversion as the red emitter for white light, however in the Eu^{3+} concentrations studied it was not bright enough for the application [32]. We then followed up that work by trying to increase the Eu^{3+} concentration in red emitting α-$(Ag_{2-3x}Eu_x)WO_4$ (x = 0.01–0.08 mol) phosphor to further assess its' potential for use in new applications based on its' nano-rod morphology which allows for preferred alignment, dense packing and directional emission characteristics (we have reported the X-ray powder diffraction data and the Raman spectra of these materials but not their emission spectra which we will report

herein) [2]. The second topic covered by this paper is an approach that involves the use of a co-dopant. The rational for the latter partially discussed above is also based on the fact that a number of alkali-metal ion (Li, Na, and K)Eu^{3+} tungstate phosphors have been reported [9–13,15,18] where the alkali metal and the Eu^{3+} cations are on the same lattice site. So as this approach can reduce the amount of Eu^{3+} cations needed to produce better and more efficient phosphors we also report the effect of introducing both Li^+ and Eu^{3+} into the α-Ag_2WO_4 lattice at the same time according to the formula of α-$(Ag_{2-3\times-y}Eu_xLi_y)WO_4$ (where x = 0.01, y = 0.01–0.03 mol).

A further aim of this work was to further understand how the Eu^{3+} site occupation in these phosphors affects their photoluminescence properties. To this end in addition to their excitation and emission spectra, the luminescence decay lifetimes of the emitting $^5D_0$ level of the Eu^{3+} ions were also studied.

2. Experimental and methods

2.1. Synthesis

The α-$(Ag_{2-3\times}Eu_x)WO_4$ (x = 0.01–0.08 mol) phosphor nanorods were efficiently synthesized via a low temperature (90 °C) coprecipitation (CP) method [2,32]. The α-$(Ag_{2-3\times-y}Eu_xLi_y)WO_4$ (where x = 0.01, y = 0.01–0.03 mol) phosphor nanorods were synthesized in a similar way. For the latter In a typical experiment, 1.0 mmol of $Na_2WO_4{\cdot}2H_2O$ (Aldrich, 99%) and 2.0 mmol of $AgNO_3$ (Aldrich, 99%) were dissolved separately in 50 mL of deionised water at 90 °C under magnetic stirring for 5 min. $Eu(NO_3)_3$ and $LiNO_3$ stock solution was obtained by dissolving Eu_2O_3 (Aldrich, 99.999%) and Li_2CO_3 in dilute nitric acid and stoichiometric added to the Silver solution. Then, the solutions were mixed together at 90 °C under constant stirring for 30 min. These crystals were obtained as a fine white powder precipitated at the bottom of the glass flask after turning off the stirring. The precipitates were washed with deionized water to remove any remaining sodium and nitrate ions. Finally, the crystals were collected and then dried in an oven at 80 °C for 6 h. The nanorods emitted red light without further heat treatments.

2.2. Characterisation

2.2.1. X-ray powder diffraction

The nanorods were structurally characterised using: X-ray powder diffraction d (XRPD) data analysed by Rietveld refinement and low temperature (20 °C to −190 °C) micro-Raman spectroscopy as previously described [2]. The morphology of the nanorods was confirmed by field emission scanning electron microscopy. XRPD of the samples was obtained using a Bruker D8 Advance X-ray powder diffractometer fitted with a copper source and LynxEye™ silicon strip detector. The LynxEye detector is a position sensitive, silicon based, semiconductor detector. Powder samples were loaded into plastic holders which were rotated during the measurements which last up to 3 h. The rotation reduces any preferential orientation that would exist in the powder sample. The greater length of time reduces the background noise, especially prevalent in lower angle detection. The diffractometer was previously calibrated using an aluminium oxide line position standard from Bruker and the NIST SRM 660a (LaB_6) line profile standard. The emission of the nickel filtered Cu source and hence the instrumental line broadening was determined by fitting the NIST standard using the software Bruker TOPAS version 5. The samples were scanned from 5° to 100° (2θ) for 35 min in step scan mode (0.01°).

2.2.2. Micro-Raman spectroscopy

Micro-Raman spectroscopy was carried out using a Horiba Jobin Yvon LabRAM HR800 spectrometer. The instrument has a built-in He-Ne 20 mW laser of 632.8 nm wavelength, which is polarized at 500:1. In addition there is an Ar^+ green laser of 532.01 nm wavelength. One air-cooled CCD detector is set for collecting signals in the visible light region and one liquid nitrogen cooled CCD detector for those in the infrared region. Luminescence spectra were recorded using the aforementioned LabRAM Raman spectrometer equipped with a HeNe laser operating on the 532 and 633 nm line. The samples were placed on a silica slide with slight pressure to give a flat surface before being placed on the microscope stage. Once calibration was carried out, the laser was focused on the sample. Multi-window accumulation mode was used to record the spectra. For Raman spectra, data was collected from 50 to 1100 cm^{-1}. For UC and DC PL emission spectra were collected from 400 nm to 900 nm using 532 nm and 633 nm notch filters. The luminescence study was based on the excitation and emission spectra recorded at room (300 K) temperature.

2.2.3. Photoluminescence spectra

PL emission and excitation spectra of the samples were recorded using a Horiba Yobin Yvon Flurolog®-3 spectroflurometer under excitation of a 450 W xenon lamp. Data were collected by the FluroEssence software. Luminescence decay curves were recorded in a SPEX1934D phosphorimeter accessory with a 150 W pulsed lamp.

2.2.4. Field emission scanning electron microscopy

Field emission scanning electron microscopy (FESEM) was used to determine particle size and morphology of the samples using a Carl Zeiss Supra 35 VP instrument. Standardised magnifications were used to allow direct comparison between each sample. These images were exported directly and are shown with the specific bar scale for each sample. Carbon conducting tape was fixed on aluminium stubs, which were then coated with the material.

3. Results and discussion

Previously [2] we reported the XRPD patterns of α-$(Ag_{2-3\times}Eu_x)WO_4$ samples. All of the peaks observed were indexed to the pure orthorhombic phase of α-Ag_2WO_4 (PDF no 34–0061(ICSD no 4165)). These results indicated that the Eu^{3+} cations had been introduced efficiently into the α-Ag_2WO_4 lattice until 4 mol% Eu^{3+}. In the sample containing 8 mol% Eu^{3+} small peaks related to Silver Europium Tungsten Oxide (PDF no 60–0818) were observed. This was evidence of saturation of the α-Ag_2WO_4 orthorhombic structure by the Eu^{3+} cations [2].

Fig. 1 presents the XRPD patterns of α-$(Ag_{2-3\times-y}Eu_xLi_y)WO_4$ samples. Again all of the peaks observed in the patterns can be indexed to the pure orthorhombic phase of α-Ag_2WO_4 and are in good agreement with ICSD no 4165. These results indicate that Eu^{3+} and Li^+ ions have both been introduced efficiently into the α-Ag_2WO_4 lattice. Peaks related to Ag_2O or Eu_2O_3 phase were not detected, which is evidence of the efficient and uniform incorporation of both Eu^{3+} and Li^+ cations into the host lattice due in the former case to the similar ionic radii of Eu^{3+} and Ag^+ (1.22 Å and 1.087 Å, respectively). The difference in the ionic radii obeys Vegard's law [57] and this establishes a limit of around 15% to obtain complete solid solubility between the dopant and the host matrix ion [2]. Also, the time and temperature of synthesis were not sufficient to reduce Ag^+ to Ag as no extra reflection peaks that could be assigned to metallic Ag were detected. In addition, no reflections arising from the $Eu_2(WO_4)_3$ phase were observed, indicating the efficient synthesis of the α-Ag_2WO_4 phosphors as single phase. This result confirms the crystallinity and the structural order at long range of all solid solution samples without the presence of secondary phases which also contribute for better luminescence efficiency. It can therefore be concluded that the co-incorporation of both Li^+ and Eu^{3+} has enabled more Eu^{3+} to be incorporated into the α-Ag_2WO_4 than we previously were able to with just the Eu^{3+} cations alone.

As we previously explained [2] the substitution of monovalent Ag^+ cations by trivalent Eu^{3+}cations causes strain in the lattice, because for every Eu^{3+} cation occupying an Ag^+ cation site two more Ag^+ cations have been displaced from the lattice leaving two cationic sites vacant.

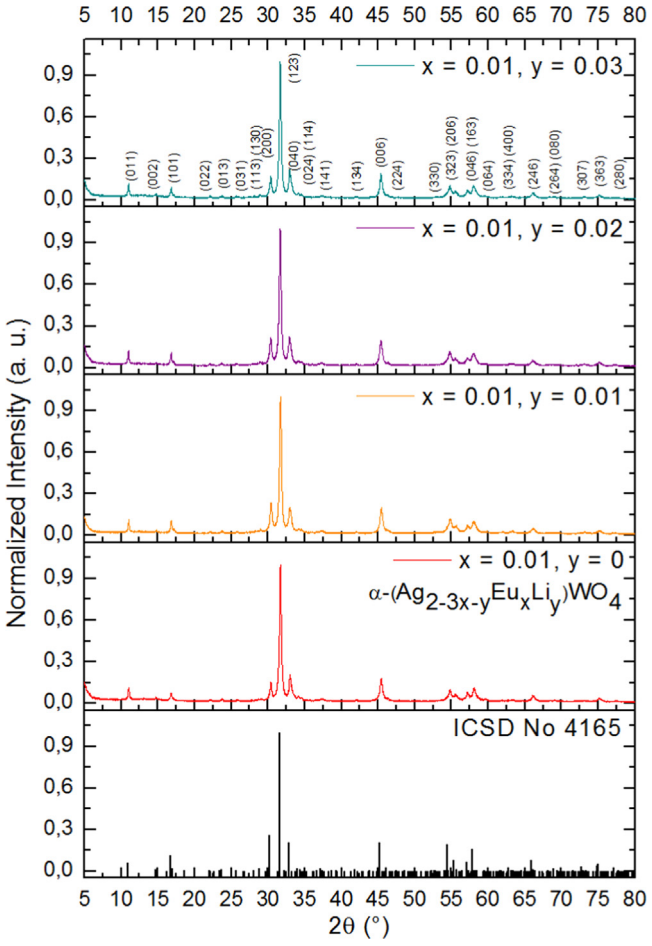

Fig. 1. X-ray diffraction patterns of α-$(Ag_{2-3\times-y}Eu_xLi_y)WO_4$ samples synthesized by the CP method at 90 °C for 30 min.

This maintains charge compensation in the lattice but both the vacancies and the Eu^{3+} charged cations cause strain. Evidence for this came from the fact that as the proportion of the Eu^{3+} cations was increased there was rejection from the lattice [2]. Thus we established that in the α-$(Ag_{2-3\times}Eu_x)WO_4$ structure x cannot be tolerated much above 4 mol%. So, in this lattice charge compensation can only be tolerated to a small extent. In fact at 4 mol% Eu^{3+}, 12 mol% of Ag^+ cations have been removed (that is around one sixteenth of the Ag^+ cations present). Though the ionic radius of Ag^+ is 1.22 Å, and that of Eu^{3+} is 1.087 Å the latter will tend to distort the crystal site normally occupied by the former because of its greater charge [58,59].

In the case of the α-$(Ag_{2-3\times-y}Eu_xLi_y)WO_4$ (where x = 0.01, y = 0.01–0.03 mol) samples structural refinement data confirm the orthorhombic structure with a *Pn2n* symmetry space group. Using the Rietveld refinement method the lattice parameters and unit cell volumes were calculated and are shown in Table 1. This table shows low deviations of all the statistical parameters which is indicative that the refinement results are quite reliable. These results were obtained by keeping the occupancy of W^{6+} fixed to 1 while Eu^{3+} and Li^+ cations were set to share occupancies in the same Ag^+ site.

As discussed above the substitution of monovalent Ag^+ ions by trivalent Eu^{3+} ions can unbalance the charge of the system due to Ag^+-vacancies or O^{2-} ions close to interstitial sites. So, in this work we made use of charge compensation to avoid distortion of the Eu^{3+} sites that in consequence can interfere with the PL emission. Thus the introduction of the smaller Li^+ cations (ionic radii Ag^+ = 1.22 Å, Li^+ = 0.76 Å and Eu^{3+} = 1.087 Å) can be used as a way to offset some of the lattice distortion as it should cause a contraction of the lattice. The Li^+ cations contribute to the relaxation of the host lattice and to a better insertion

Table 1
Lattice parameters, unit cell volume and statistical parameters of quality of α-$(Ag_{2-3\times-y}Eu_xLi_y)WO_4$ samples; (a) x = y = 0, (b) x = 0.01, y = 0, (c) x = 0.01, y = 0.01, (d) x = 0.01, y = 0.02 and (e) x = 0.01, y = 0.03.

	α-$(Ag_{2-3\times-y}Eu_xLi_y)WO_4$				
	(a)	(b)	(c)	(d)	(e)
a (Å)	10.8799(3)	10.875(4)	10.8799(6)	10.8803(5)	10.8772(6)
b (Å)	12.0164(5)	12.024(4)	12.0218(7)	12.0200(7)	12.0215(7)
c (Å)	5.8911(2)	5.899(2)	5.8910(3)	5.8920(3)	5.8943(4)
Cell volume ($Å^3$)	770.19(5)	771.3(5)	770.52(7)	770.57(7)	770.74(8)
R_{exp} (%)	7.53	7.15	7.24	7.02	7.04
R_{wp} (%)	16.0	14.90	10.74	10.54	10.90
R_p (%)	12.36	11.17	8.33	8.23	8.49
R_{Bragg} (%)	6.380	6.349	2.026	2.026	2.232
Crystal size (nm)	32.98(16)	22.84(16)	33.20(14)	33.10(14)	32.62(14)

of the Eu^{3+} ions. The presence of this ion can also prevent the formation of crystal defects and lattice stress, which can lead to a decrease in the luminescence of the material. Hence the introduction of some Li^+ cations can limit/compensate for the lattice distortion caused by the presence of the Eu^{3+} sites and this will be supported later in the discussion of the PL emission. It should be noted that it is highly improbable that the Li^+ cations can occupy W^{6+} (r = 0.60 Å) sites because of the latter's smaller ionic radius and higher electronic charge.

The full width half the maximum of peaks in the diffraction data slightly decrease and the peaks are sharper for the samples co-doped with Li^+. This indicates the higher crystallinity of these samples. As discussed above charge balance neutrality of the α-$(Ag_{2-3\times-y}Eu_xLi_y)WO_4$ samples is achieved by Ag^+ vacancies due to Eu^{3+} doping by reaction (1):

$$3Ag_{Ag} + 1Eu_{Eu} \rightarrow 1Eu_{Ag} + 2V_{Ag} \quad (1)$$

where Ag_{Ag} is silver in the AgO_n lattice, Eu_{Eu} is europium in the EuO_n lattice, Eu_{Ag} is the Eu ion substituted into Ag^+ sites and V_{Ag} is the silver vacancy. In Eq. (1) it is obvious that two vacant cation sites are caused whenever an Eu^{3+} cation replaces $3Ag^+$ cations. So three sites are affected and two vacancies are produced this can be considered as a ratio of 2:3. The relative amount of Ag vacancies and the disruption to the lattice is minimised by using the smaller Li^+ cations as a co-dopant as shown by the reaction (2):

$$4Ag_{Ag} + 1Eu_{Eu} + 1Li_{Li} \rightarrow 1Eu_{Ag} + 1Li_{Ag} + 2V_{Ag} \quad (2)$$

As in this case four lattice sites are affected and only two vacancies arise. So four sites are affected and two vacancies are produced this can be considered as a ratio of 2:4. Thus the lattice is less disturbed by the substitutions. This process is responsible for the increase of the crystallinity and long-range order of the samples [60], as it should be realised that the Li^+ cations are much smaller than the Ag^+ cations so they cause compression in the structure.

The unit cell volumes and crystallite sizes (see Table 1) show slight difference because of the substitution of silver by europium and lithium ions. The crystallite sizes calculated from the line broadening of the powder diffraction data and extracted using Bruker Topas 5 software assuming spherical particles.

All three cells that contain Li^+ cations as well as Eu^{3+} cations have larger cell volumes than that of pure α-Ag_2WO_4, but smaller than that of α-$(Ag_{2-3\times}Eu_x)WO_4$ (where x = 0.01 mol.). The fact that the doping with Eu^{3+} cations increases the unit cell volume suggests that this is due to the charge on these cations distorting the lattice as on a size basis this cation is smaller than Ag^+ and it may have been expected to make the lattice smaller. When Li^+ cations are added the cells are smaller than the cell containing just Eu^{3+} cations alone, this is because these much smaller cations counteract the Eu^{3+} charge distortions. Besides

their dissimilar ionic radii, Eu^{3+} ions have higher and Li^{+} lower electron density, respectively, that may causes disturbance in the silver polyhedral [AgO_n] (n = 2, 4, 6 and 7) contributing for the differences observed in the cell volumes. In addition, Eu^{3+} and Li^{+} substitutions may cause formation or reduction of structural defects (oxygen vacancies, distortion on the bonds, leading to stresses and strains on the crystalline lattice) that may also contribute to the small changes observed. In Table 1 the refinement of the α-Ag_2WO_4 sample synthesized by the same procedure is included for comparison.

The crystallinity of the samples can be evaluated from the crystallite sizes; these values are also shown in Table 1. Usually, the larger crystallite size means higher crystallinity. At first glance, the undoped sample has a larger crystallite size compared to the doped ones. However, the samples α-$(Ag_{1.97-y}Eu_{0.01}Li_y)WO_4$ presents the largest crystallite size due possibly to the optimal Li^{+} concentration. This larger value reflects the reduction of defect sites where the photo-excited electrons are consumed without luminescence. It is well known that the generation of oxygen vacancies affects the crystallinity and thus the luminescence. The high Eu^{3+} concentration favours the creation of oxygen vacancies due to reduction of Eu^{3+} symmetry when doping Ag^{+} sites [61].

3.1. Unit cell representation

The unit cell´s representations of the orthorhombic α-Ag_2WO_4 and α-$(Ag_{1.95}Eu_{0.01}Li_{0.02})WO_4$ nanocrystals are illustrated in Figs. 2 and 3, respectively. The unit cell was modelled through *Visualization for Electronic and Structural Analysis* (VESTA) [62] program (3.3.8 for 64-bit version of Windows®), using the lattice parameters and atomic positions obtained from the Rietveld refinement data presented in Table 1. The α-Ag_2WO_4 unit cell consists of distorted WO_6 polyhedrons with octahedral configuration. There are three different polyhedrons containing W atoms (W1, W2 and W3), and all are coordinated to six O atoms. The Ag atoms can have four types of coordination: i) Ag1 and Ag2 atoms are coordinated by seven O atoms (AgO_7 deltahedral polyhedrons); ii) Ag3 atoms are coordinated by six O atoms (AgO_6 octahedral polyhedrons); iii) Ag4 and Ag5 atoms are coordinated by four O atoms (AgO_4 tetrahedral polyhedrons) and iv) Ag6 atoms are coordinated by two O atoms (AgO_2 angular polyhedrons). When doped with Eu^{3+} and Li^{+}, these ions are supposed to be located in AgO_7 and AgO_2 clusters, respectively [32]. These substitutions are possible due to similar coordination number, electronic charge density and though smaller ionic radii of the Li^{+} dopant in relation to Ag^{+} ions.

3.2. Crystal morphology

Fig. 4 shows the crystal morphology of α-Ag_2WO_4 superimposed on its ball-and-stick structural model. In Fig. 4 the crystal faces are labelled with the indices of the (010), (101) and (001) planes and according to the literature, α-Ag_2WO_4 nanocrystals have preferentially grown in the [001] direction [35].

3.3. Field emission scanning electron microscopy

Fig. 5(a)-(d) presents the FESEM micrographs of the samples using x10000 magnification. The shape and size of these particles are almost identical to those we previously reported for the materials that contained no Li^{+} [2]. The morphology and the size distribution of the crystals of a phosphor are both important parameters that may well influence the luminous flux emitted by the particles and also the way they may lie/orientate on a surface (for device application). Ideally for many applications it would useful to have uniform sub-micron phosphor particles without any reduction in the luminous efficacy (compared to larger micrometer sized particles) [2]. Materials that have scale dimensions that are equivalent in all but one direction (length > width) are called one dimensional structures (1D structures),

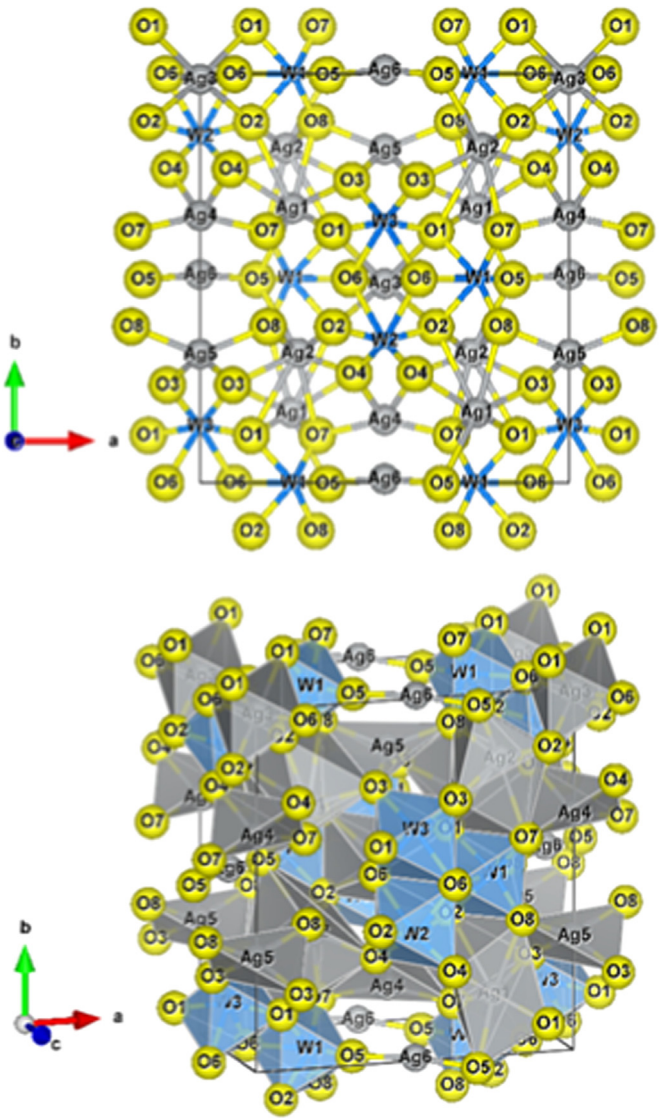

Fig. 2. Unit cell representation of α-Ag_2WO_4.

examples include rods, tubes, fibres and wire-shaped materials. Clearly the morphologies manifested in Fig. 5(a)-(d) are very rod like. These morphologies present some advantages over others 2D or 3D materials as they may facilitate preferred alignment, dense packing and directional emission characteristics for lighting application purpose. There is no evidence for strong adhesion among particles as it is possible to see clear boundaries between the particles. In all cases there is evidence for the majority of the particles having similar size and shape. These crystals are smooth surfaced nanorods of around 100 nm in width and 1–2 μm in length similar to those we previously reported [2]. It would be expected that the morphology of these nanorods should perhaps endow preferred alignment (self-assembly), in turn leading to dense packing and possibly facilitate directional emission.

There are no noticeable differences in the morphology due to the combined Li^{+} and Eu^{3+} ions doping except in the sample with 0.02 mol Li^{+}. This sample manifests a reduction on the average length 1 μm (to around 0.7 μm) and no changes in width. The modification in the size of the material is concomitant with an increase in crystallite size as seen from the fit of the XRD powder data (Table 1). The reasons why this material is out of line are unclear. However, the cell size may be out of line because of the amount of Li^{+} cations present that may have been ordered during the synthesis in empty Ag^{+} lattice sites to maximize charge balance. When more Li^{+} is present the cell becomes smaller. As

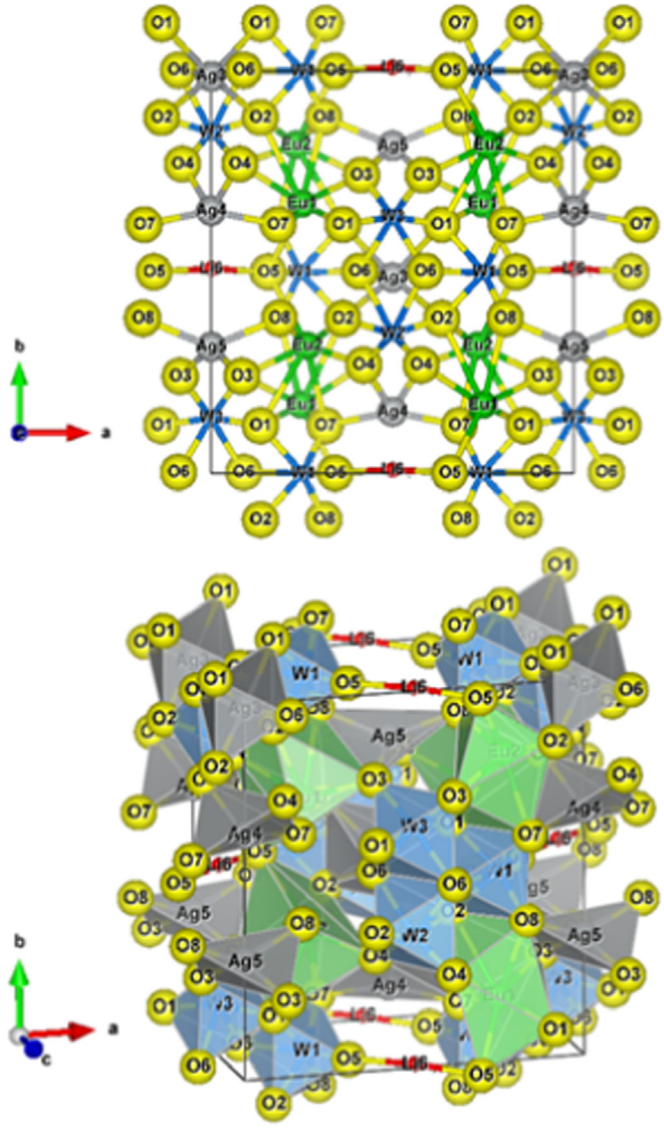

Fig. 3. Unit cell representation of α-$(Ag_{1.95}Eu_{0.01}Li_{0.02})WO_4$, indicating the possible Eu^{3+} and Li^+ sites.

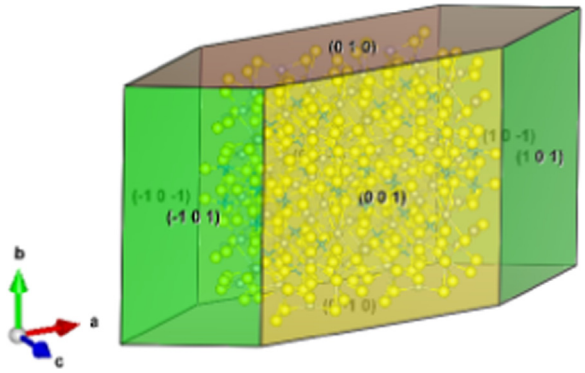

Fig. 4. Crystal morphology of α-Ag_2WO_4 superimposed on its ball-and-stick structural model.

will be discussed below the variation in spectral properties of the samples may result from changes in the crystal fields on the Eu^{3+} cations in the lattices as more or less Li^+ cations are present rather than because of the crystallinity or morphology [63].

3.4. Micro-Raman spectroscopy

We have previously reported the Raman spectra of the α-$(Ag_{2-3\times}Eu_x)WO_4$ (x = 0–0.08 mol) samples [2]. Raman spectra are useful for studying parameters that affect the luminescence efficiency of phosphors. The crystallographic phases present, lattice phonon energies, and the site symmetries of activators may be studied by this technique [64]. It has been shown that α-Ag_2WO_4 belongs to the C_{2v}^{10} space group and has two molecular formulas per unit cell (Z = 2). Though group theory predicts that there should be 21 different Raman modes [2,65], only 14 modes were previously identified [2,32].

In Figs. 6 and 7 the room temperature Raman spectra of the α-$(Ag_{2-3\times-y}Eu_xLi_y)WO_4$ (where x = 0.01, y = 0.01–0.03 mol) samples excited at 532 and 633 nm, respectively are presented. These spectra are very similar to those reported and assigned for the α-$(Ag_{2-3\times}Eu_x)WO_4$ (x = 0.0–0.01 mol) phosphor samples [32] and also to those for the α-$(Ag_{2-3\times}Eu_x)WO_4$ (x = 0–0.08 mol) samples [2]. The differences in the Raman spectra presented here in Figs. 6 and 7 to those presented in references [2,32] arise from the presence of emission bands emanating from the larger Eu^{3+} cation concentration present both in the samples studied in this work and those we reported previously [2], Evidence in support of this will be discussed later. The assignments of the Raman spectra presented in Figs. 6 and 7 are listed in Table 2. The assignments of the Raman modes below 251 cm^{-1} have been discussed in detail previously [2] and we refer the interested reader to it. All the Raman bands listed here can be explained as presented in ref 2.

For the sample with 2 mol% of Li^+ the $A_{1\,g}$ mode at 883 cm^{-1} was the most well defined and sharp mode compared to the others samples; this mode observed at 883 cm^{-1} is from the symmetric stretching of W-O [2,66]. Although this mode is present in all three Li^+ containing samples it is most prominent in the sample with 2 mol% of Li^+ and was less well defined in the samples without Li^+, see Figs. 6 and 7 and also those in ref. [2]. It has to be the presence of the Li^+ cations that cause this bands enhancement and are associated with a change in the bonding of the lattice as the latter cations replace Ag^+ cations. In other tungstate lattices Li^+ and Eu^{3+} occupy the same lattice sites. These results shows that Li^+ decreased the tension caused by the inclusion of the Eu^{3+} in the material resulting in better defined Raman modes for this sample [16,67,68].

The room temperature Anti-Stokes and Stokes luminescence and Raman spectra of the α-$(Ag_{2-3\times-y}Eu_xLi_y)WO_4$ (x = 0.01, y = 0.01–0.03 mol) samples excited at 532 and 633 nm respectively are presented in Figs. 8 and 9. As discussed in ref 2 the strongest Raman modes typical of α-Ag_2WO_4 are seen on both anti-Stokes and Stokes sides of the spectra. Also as stated in Ref. [2] the characteristic emission bands presented in Figs. 8 and 9(f-f peaks of Eu^{3+}) at around 591, 616, 652 and 702 nm, are due to the $^5D_0 \rightarrow {}^7F_1$, $^5D_0 \rightarrow {}^7F_2$, $^5D_0 \rightarrow {}^7F_3$ and $^5D_0 \rightarrow {}^7F_4$ [2,69]. In the spectra shown in Fig. 9 excited at 633 nm the emission bands at higher energy arise from a combination of the energy of the laser line plus the thermal energy of the electrons in the ^7F_j states [69]. In Fig. 8 where the spectra result from 532 nm excitation the higher energy emission bands may arise from a similar process or alternatively (but less likely) they may be excited by a two photon UC process as suggested in Ref. [2] for the none Li^+ doped material.

The emission bands are markedly intense for the sample α-$(Ag_{1.95}Eu_{0.01}Li_{0.02})WO_4$ using 0.1% filter (by a factor of 1000 compared to the other samples). These more intense and sharp peaks are probably caused by the relaxation of the host lattice allowing Eu^{3+} ions to be more easily located in the silver sites at this stoichiometry. This finding of course suggests that at the other stoichiometries the lattices are not ideal for Eu^{3+} luminescence [70]. It is therefore proposed that the creation of cation vacancies by the inclusion of Eu^{3+} cations on the Ag^+ cation sites is very disruptive in the lattice but that this can be offset by the exchange of some Ag^+ cations by smaller Li^+ cations. The radius discrepancy between other alkali-metals (Na^+ and K^+) and Ag^+ cations is disadvantageous to the enhancement of Eu^{3+} luminescence.

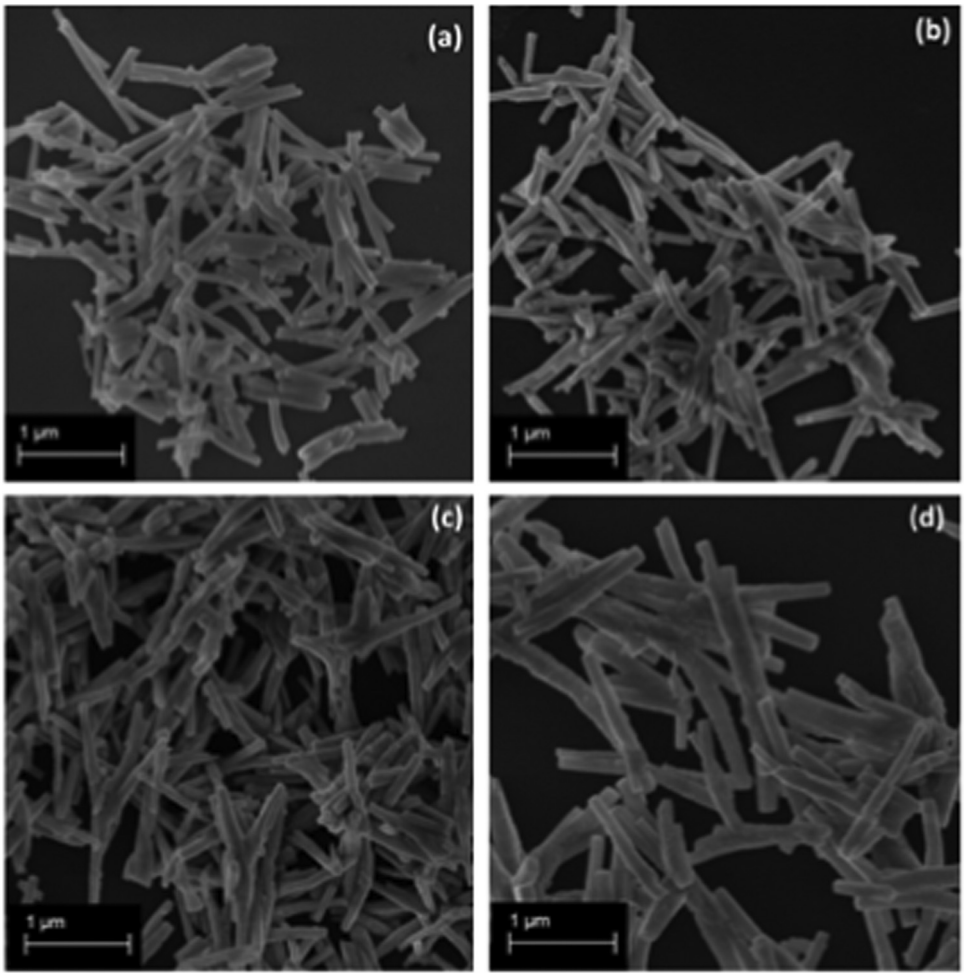

Fig. 5. SEM micrographs of α-$(Ag_{2-3\times-y}Eu_xLi_y)WO_4$ samples synthesized by the CP method at 90 °C for 30 min. (a) x = 0.01, y = 0; (b) x = 0.01, y = 0.01; (c) x = 0.01, y = 0.02 and (d) x = 0.01, y = 0.03.

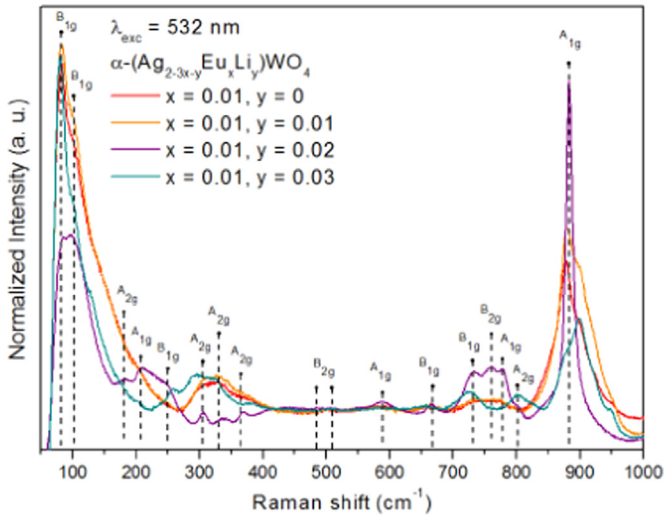

Fig. 6. Raman spectra of the samples α-$(Ag_{2-3\times-y}Eu_xLi_y)WO_4$ (x = 0.01, y = 0.01–0.03) excited at 532 nm.

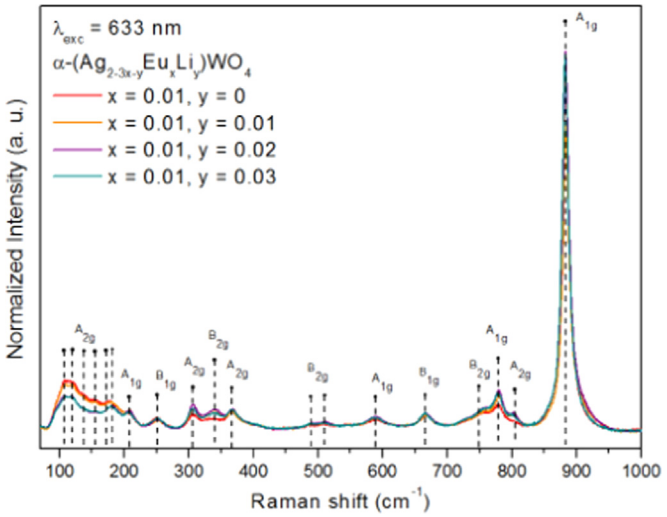

Fig. 7. Raman spectra of the samples α-$(Ag_{2-3\times-y}Eu_xLi_y)WO_4$ (x = 0.01, y = 0.01–0.03) excited at 633 nm.

Thus, we can assume that smaller lattice distortions are created when Li^+ is used instead of others alkali metals (Li^+ - 0.92 Å, Na^+ - 1.18 Å and K^+ - 1.51 Å) [71,72].

In Fig. 10 the temperature dependence of the Raman spectra of α-$(Ag_{1.95}Eu_{0.01}Li_{0.02})WO_4$ excited at 532 nm are shown. It is apparent that as the temperature decreases an improvement in the definition of the Raman modes occurs and the most likely explanation is that this is due to less lattice vibrations at lower temperatures. This is a reflection of a reflection of a more organised structure containing 2 mol%Li^+ that does not facilitate energy loss.

Table 2
Raman modes assignments for α-$(Ag_{2-3\times-y}Eu_xLi_y)WO_4$ nanocrystals.

Mode position (cm^{-1})	Assignment
107w	T′(Ag^+/W^{6+})
120w	
138w	
155w	
182w	
208w	
251w	
306w	δ (WOOW) out-of-plane bending
340m	δ_s (O–W–O)* δ (WOOW)* δ (W–O–W)
367w	
489vw	δ (WOOW) out-of-plane wagging
510vw	
589m	δ_{as} (W–O–W)* δ (WOOW)
666m	ν_s (WOOW)
749vw	ν_s (WOOW)* ν_s (W–O)
779s	ν_{as} (W–O)
805vw	ν_{as} (W–O–W)* ν_{as} (W–O)
883vs	ν_s (W=O)

Abbreviations: vs – very strong, s – strong, m – medium, w – weak, vw – very weak, νs – symmetric stretch, νas - asymmetric stretch, δs – symmetric bend, δas – asymmetric bend, T′ – translational.

* coupling of vibration.

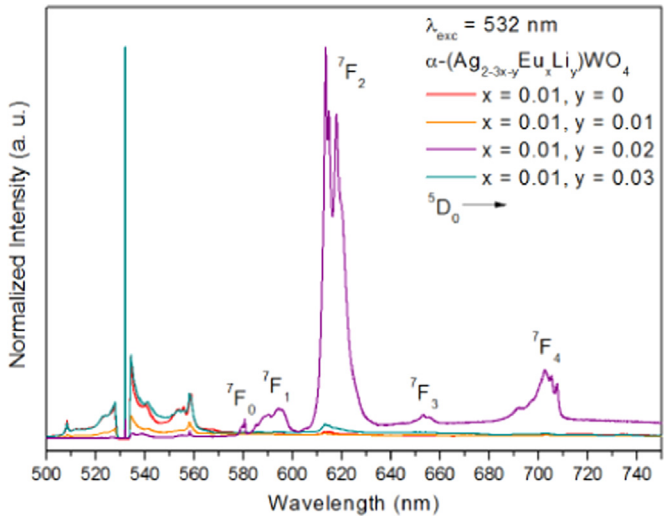

Fig. 8. PL-Raman spectra of the samples α-$(Ag_{2-3\times-y}Eu_xLi_y)WO_4$ (x = 0.01, y = 0.01–0.03) excited at 532 nm.

Fig. 11 presents the temperature dependence of the Stokes emission spectrum of α-$(Ag_{1.95}Eu_{0.01}Li_{0.02})WO_4$ excited at 532 nm. The intensities of all of the Stokes luminescence lines are seen to be temperature-dependent. As this material gave the Stokes emission spectrum seen in Fig. 8 that was 1000 times stronger than those of the other Li^+ materials it is worth examining it's temperature behaviour. The intensity of the main emission ($^7F_2$) is seen to decrease with temperature and at the lowest temperature (-190 °C) the relative intensities of the $^7F_2$ lines swap over compared to the + 20 °C temperature. This lowering of intensity with temperature is not uncommon and may indicate a structural change of some sort, this would also explain the change in the relative intensities of the lines.

3.5. Photoluminescence properties

The emission and excitation bands of Eu^{3+} cations are influenced by the crystallographic site(s) on which they are located in a given host lattice and the resulting spectra can give information about the coordination of the activator and its surroundings. Excitation and

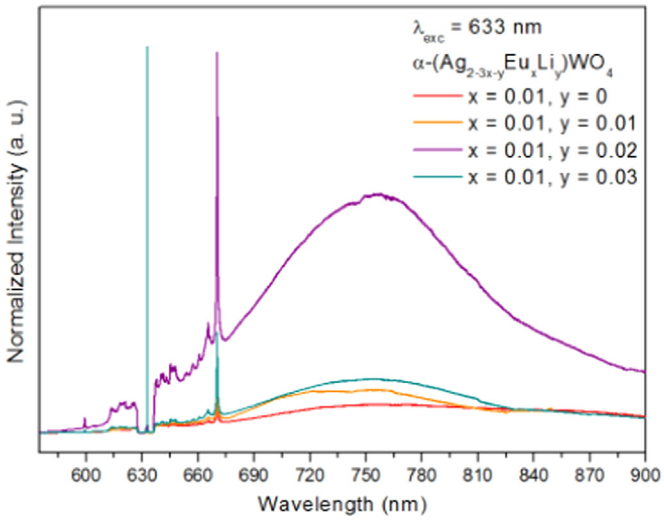

Fig. 9. PL-Raman spectra of the samples α-$(Ag_{2-3\times-y}Eu_xLi_y)WO_4$ (x = 0.01, y = 0.01–0.03) excited at 633 nm.

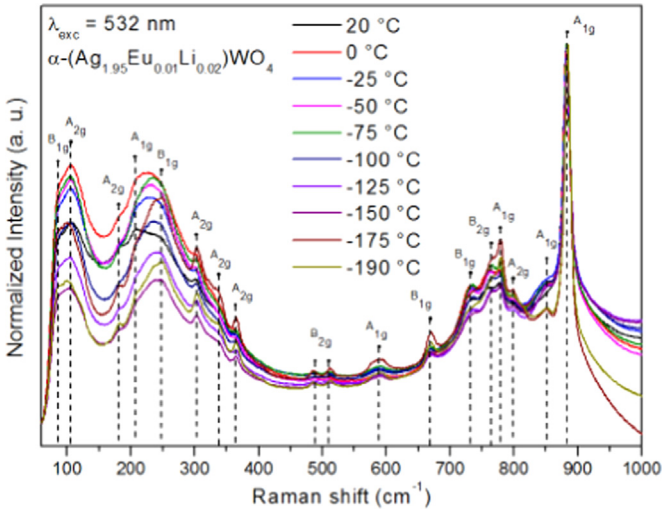

Fig. 10. Temperature-dependent Raman spectra of α-$(Ag_{1.95}Eu_{0.01}Li_{0.02})WO_4$ excited at 532 nm.

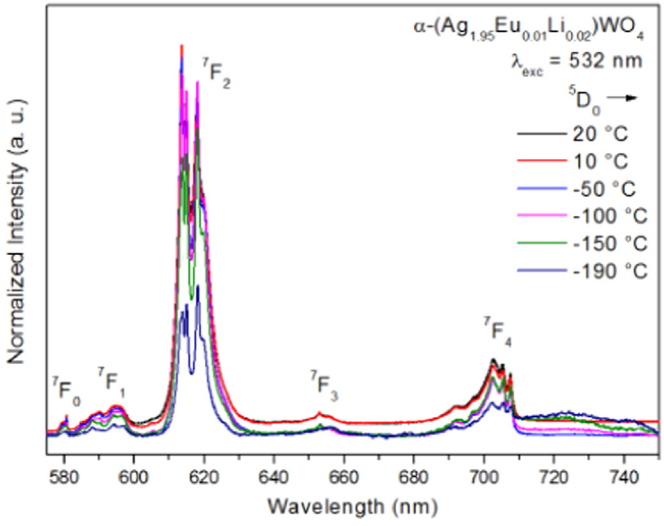

Fig. 11. Temperature-dependent PL-Raman spectra of α-$(Ag_{1.95}Eu_{0.01}Li_{0.02})WO_4$ excited at 532 nm.

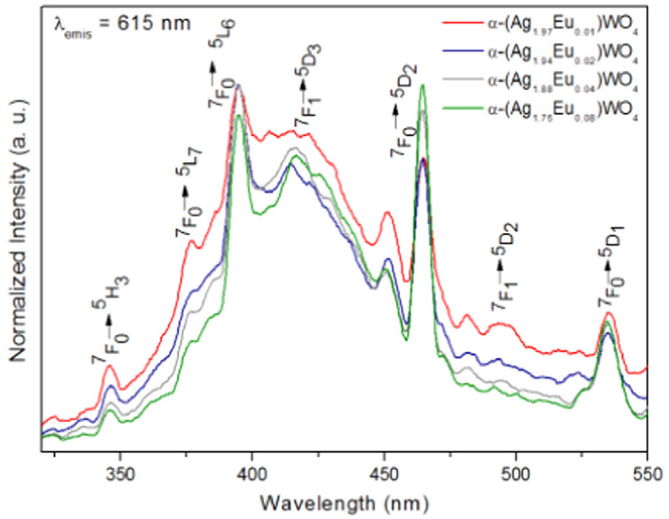

Fig. 12. Excitation spectra of α-$(Ag_{2-3\times}Eu_x)WO_4$ (x = 0.01–0.08) monitored at 615 nm.

emission spectra of the samples were measured using a Xe lamp.

Fig. 12 presents the excitation spectra of α-$(Ag_{2-3\times}Eu_x)WO_4$ (x = 0–0.08 mol) samples monitored using 615 nm emission band. The excitation spectra consist of a broad band extending from 350 to 500 nm centred at 425 nm and some smaller sharper bands. The former is due to the charge transfer from the ligand to the metal (LMCT) which is derived from the $^1T_1$–$^1A_1$ transition of O^{2-}→W^{6+} in the WO_6 group and also charge transfer of (2p) O^{2-}→Eu^{3+} (4f).

Overall, the contribution of these two bands cannot be distinguished because of the spectral overlap. However this is explained further below considering the spectra of the α-$(Ag_{2-3\times-y}Eu_xLi_y)WO_4$ (x = 0.01, y = 0.01–0.03 mol) samples shown in Fig. 13.

Fig. 13 shows the excitation spectra α-$(Ag_{2-3\times-y}Eu_xLi_y)WO_4$ (x = 0.01, y = 0.01–0.03 mol) samples recorded in the 320–600 nm range monitoring the hypersensitive $^5D_0$→$^7F_2$ transition of Eu^{3+} at 615 nm. These spectra are very similar to those of the α-$(Ag_{2-3\times}Eu_x)WO_4$ (x = 0–0.08 mol) samples and like them, they consist of an intense broad band in the interval range from 320 to 400 nm, with a maximum at 400 nm due to the overlap of the charge transfer (CT) bands from oxygen to europium (O–Eu) at 265 nm and/or tungsten (O-W) at around 310 nm, which is derived from the $^1T_1$– $^1A_1$ transition of O^{2-} → W^{6+} in the WO_6 group [2]. Once more the contribution of these two

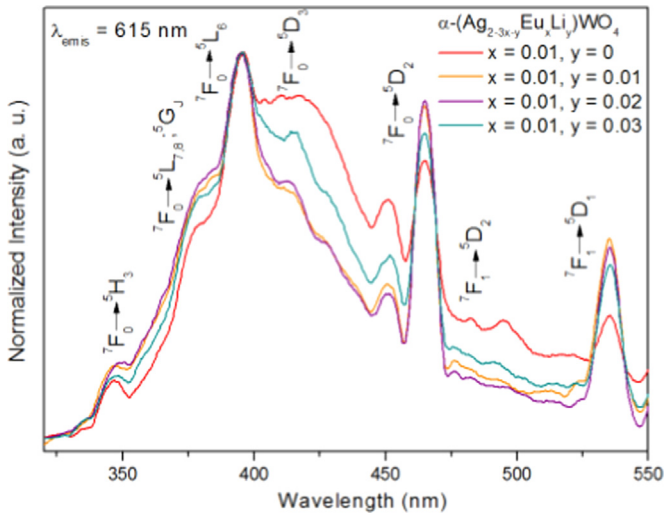

Fig. 13. Excitation spectra of α-$(Ag_{2-3\times-y}Eu_xLi_y)WO_4$ samples monitored at 615 nm.

bands cannot be distinguished because of the spectral overlap. This overlap may be due to the electron transfer from 2p state of oxygen (near the top of the valence band) to the 4d state of tungstate (near bottom of the conduction band) by absorption of the photons after excitation. The electrons at this excited state finally decay to lower energy states by radiative transitions [7]. In α-$(Ag_{2-3\times}Eu_x)WO_4$ phosphors, the CT is related to electron transitions from the oxygen 2p orbital to the empty W^{6+} 5d orbital or to an empty Eu^{3+} 4f orbital. This band is ascribed to the coupling between the luminescence centres and the crystal lattice which mainly depends on the distance from the metal cations to the ligands [73]. The presence of the strong band of WO_4^{2-} groups in the excitation spectrum indicates that efficient energy transfer takes place from the WO_4^{2-} groups to the Eu^{3+} cations non-radiatively in α-Ag_2WO_4 [53,74]. This phenomenon is known as "host-sensitized" energy transfer.

When the W cations have higher coordination numbers, they also manifest longer and weaker W^{6+}- O^{2-} bonds and their energy is lower extending the CTB edge from 320 nm to 400 nm [75]. The CTB becomes narrower when Li^+ ions are inserted into the host lattice due to better crystal organization and changes of the crystal field surrounding the WO_6 octahedra [53]. If no such CTB shifts occur, then it may be evidence of similar ionic radii and effectiveness substitution between Ag^+ and Eu^{3+} ions, according to XRD patterns.

As stated previously the sharper excitation bands are due to f–f transitions within $4f^6$ electron of the Eu^{3+} cations [2]. The three bands centred at 395 nm ($^7F_0$→$^5L_6$) and 465 nm ($^7F_0$→$^5D_2$) and 535 nm ($^7F_1$ → $^5D_1$) are the most intense excitation bands. Less intense bands were observed at 345 nm ($^7F_0$→ $^5D_4$), 375 nm ($^7F_0$ → $^5L_{7,8}$; ^5G_J), 415 nm ($^7F_0$→ $^5D_3$), 450 nm ($^7F_1$→ $^5D_2$), 495 nm ($^7F_0$→ $^5D_1$), 578 nm ($^7F_0$→ $^5D_0$) and 590 nm ($^7F_1$→ $^5D_0$).

The band located at 394 nm ($^7F_0$→$^5L_6$) is the most intense transition, and it is forbidden by the ΔS and ΔL selection rules but allowed by the ΔJ selection rule. The intensity of the magnetic dipole allowed transition at 540 nm ($^7F_1$ → $^5D_1$) is relatively weaker than the $^7F_0$→$^5D_2$ (hypersensitive transition) induced electric dipole allowed transition at 465 nm for all the samples [76]. In addition, there is no significant change on the intensity of the peaks due to doping by Li^+ ions. Moreover, the position of excitation peaks of Eu^{3+} presents no change because the 4f electrons are shielded by the outer $5s^2$, $5p^6$ electrons and the variation of crystal field has little effect on 4f electron transition. The excitation bands listed here could be excited by ultra-violet (UV), near-UV, UVB and blue laser diodes/LEDs as pumping sources for the red emission from Eu^{3+} ions. In particular the band at 465 nm is at an ideal wavelength to be excited by blue LED light. If the phosphor were more efficient it would be a good red emitter [17,18,77].

Fig. 14 (a) and (b) presents the emission spectra recorded in the 500–750 nm range excited by $^7F_0$→$^5L_6$ transition of Eu^{3+} at 395 nm and by $^7F_0$→$^5D_2$ transition at 465 nm, respectively. To understand the emission bands present in Fig. 14 and what can be learnt from them it is useful to briefly consider some basic ideas. The 4f intra-configurational transitions are forbidden to first order by the Laporte rule. Therefore, to overcome the small absorptivity coefficients, luminescence sensitizers are used to absorb and transfer energy efficiently to the rare earth element ions. This is a key to the design of a luminescent material. According to the Laporte rule, if Eu^{3+} cation occupies a centrosymmetric site then only magnetic-dipole transitions are possible. However and if Eu^{3+} is situated in a non-centrosymmetric site both magnetic-dipole and electric-dipole transitions are possible. The magnetic dipole (MD) allowed $^5D_0$→ $^7F_1$ ($\Delta J = 1$) transition is insensitive to the site symmetry around the Eu^{3+} ions (it is allowed by all the selection rules). The $^5D_0$→ $^7F_2$ ($\Delta J = 2$) transition is a hypersensitive forced electric dipole (ED) type. This transition has ED character due to the mixture of the opposite parity $4f^{n-1}5d$ states by the crystal field components according to the Judd–Ofelt theory its' amplitude depends strongly on the local symmetry around the Eu^{3+} ions and the associated electric fields. The $^5D_0$→ $^7F_3$ transition has both MD and ED (mixed) character

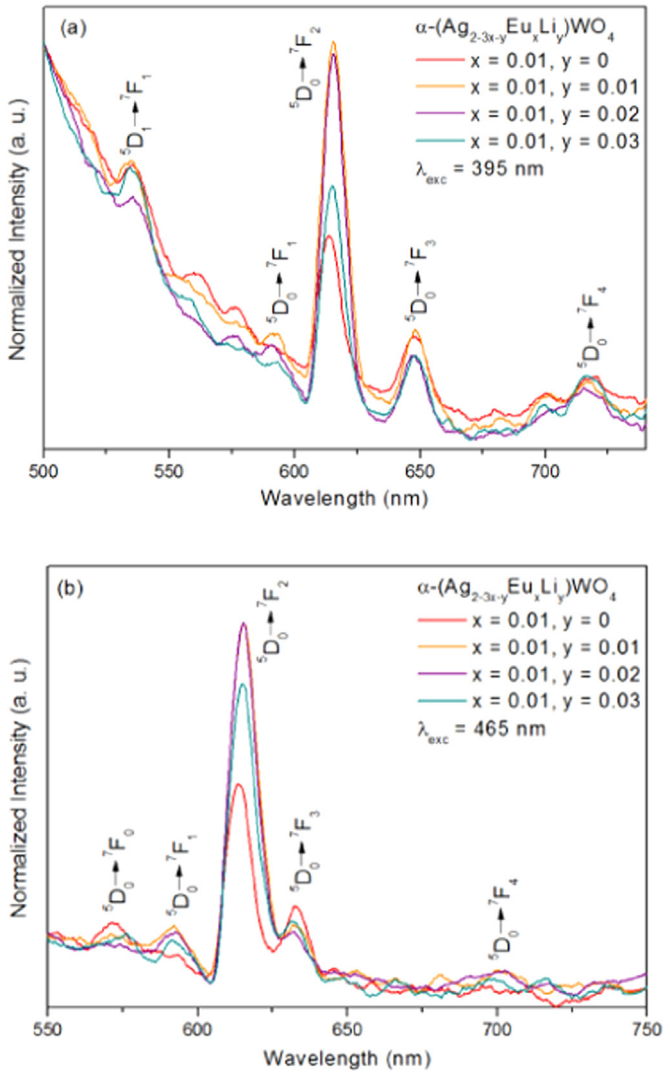

Fig. 14. Emission spectra of α-($Ag_{2-3\times-y}Eu_xLi_y$)WO_4 excited at (a) 395 nm and (b) 465 nm.

whereas the $^5D_0 \rightarrow {}^7F_4$ transition only ED. From these considerations it can be understood that when Eu^{3+} cations substitute Ag^+ sites, anion vacancies or interstitial O^{2-} defects are generated because of charge compensation effects in addition to any lattice distortion that may arise from the differences in ionic radii of the Eu^{3+} and Ag^+ cations. Thus ED transitions will be allowed due to the disordered environment and lowering of symmetry around the Eu^{3+} ions. Finally, the $^5D_0 \rightarrow {}^7F_0$ transition of Eu^{3+} is allowed only in the following 10 site symmetries: C_s, C_1, C_2, C_3, C_4, C_6, C_{2V}, C_{3V}, C_{4V} and C_{6V}, in accordance with the EDT selection rule.

Returning to Fig. 14 (a), the PL spectrum excited at 395 nm contains a background baseline below 600 nm corresponding to the transitions from the $^1A_1$ ground state to the $^1T_1$ excited state of the tungstate groups. The spectrum manifests five main emission bands centred at 580, 593, 614, 651 and 745 nm, assigned to the $^5D_0 \rightarrow {}^7F_J$ (J = 0–4) transitions of Eu^{3+}, respectively. In addition an emission band around 535 nm is apparent that results from the $^5D_1$ excited state. This is due to incomplete multi-phonon relaxation of transferred electrons from the higher excited states of Eu^{3+} to its lowest state [78]. As it is well known that $^5D_{1,2,3} \rightarrow {}^7F_J$ transitions usually appear in materials with low-lattice phonon energies, the 535 nm emission indicates the low vibration energy of tungstate group. From this deduction multi-phonon relaxation by WO_6 groups are not capable of bridging the gaps between the higher energy levels and the $^5D_0$ level of the Eu^{3+} cations completely, resulting in weak (but perceivable) emission bands from these levels. These bands are of interest for the development of host lattices manifesting high fluorescence yield.

The hypersensitive transition at 615 nm ($^5D_0 \rightarrow {}^7F_2$, ED based) is influenced by the crystal splitting surroundings and is stronger than the one at 593 nm ($^5D_0 \rightarrow {}^7F_1$, MD based). This means that Eu^{3+} ions are located in low-symmetry sites, i.e. without an inversion centre. There are four different types of Ag^+ coordination in the α-Ag_2WO_4 orthorhombic cell as discussed in the XRD section earlier. Of these sites 15% are non-centrosymmetric with C_{2v} symmetry (AgO_2), 37% are non-centrosymmetric with T_d symmetry (AgO_4), 18% are centrosymmetric with Oh symmetry (AgO_6) and 30% are non-centrosymmetric with D_{5h} symmetry (AgO_7). Taking account the size of the crystal site and its' symmetry the electric dipole $^5D_0 \rightarrow {}^7F_2$ transition in the spectra is caused specifically by the Eu^{3+} cations located at AgO_7 sites.

It is possible to see a small enhancement and a better definition of the emission peaks for the sample with 2 mol% Li^+. The materials without Li^+ cations manifest the weakest emission for the $^5D_0 \rightarrow {}^7F_2$ transition. It therefore appears that the presence of Li^+ cations is necessary to enhance the emission. 2 mol% Li^+ cations gave the greatest enhancement. Thus this crucial amount of Li^+ charge compensator contributed to the incorporation of the Eu^{3+} ions into Ag^+ sites and thus increased the emission intensity. This happens because Li^+ reduces the stress/defects of the host lattice promoting the decrease of the distortions in some optical centres where the Eu^{3+} cations are localized.

The presence of a unique, peak at 580 nm due to the $^5D_0 \rightarrow {}^7F_0$ transition also indicates single low symmetry site occupancy of Eu^{3+} in the host lattice. In addition, this transition provides information on the bonding environment and coordination of Eu^{3+} ions once there is no crystal field splitting of the $^5D_0$ and $^7F_0$ levels. The broadening of this transition is influenced by electron–phonon coupling and ion–ion interaction [67]. The 580 nm bands manifests relatively narrow width which means that Eu^{3+} ions are uniformly distributed in the host in only one type of tight crystal site. These results also attest for the high purity of the tungstate [67].

By using different excitation wavelengths (such as in this case 395 and 465 nm, see Fig. 14), it is often possible to deduce if there is overlap between of some Eu^{3+} transitions such as $^5D_0 \rightarrow {}^7F_0$ and $^5D_2 \rightarrow {}^7F_5$, $^5D_0 \rightarrow {}^7F_2$ and $^5D_1 \rightarrow {}^7F_4$, $^5D_0 \rightarrow {}^7F_3$ and $^5D_1 \rightarrow {}^7F_5$ [79]. The lower excitation energy (465 nm), populate lower excited states on the Eu^{3+} ions. So, it would be possible to distinguish in the emission spectra transitions starting at higher energy excited states that are superimposed with the ones starting at $^5D_0$. There are two noticeable differences in the emission spectra excited at 395 and 465 nm as observed in Fig. 14, the bands assigned to $^5D_0 \rightarrow {}^7F_3$ and $^5D_0 \rightarrow {}^7F_4$ under 395 nm excitation are not apparent under 465 nm excitation. Instead there is a new band at 632 nm and a small band at 701 nm. The band at 701 nm may be present in the spectrum excited by the 395 nm but it is masked by the 745 nm band. It therefore appears that the band we first ascribed to the $^5D_0 \rightarrow {}^7F_3$ transition in the 395 nm spectrum is in fact due to a higher energy transition and the band at 632 nm in the spectrum excited by 465 nm is the real $^5D_0 \rightarrow {}^7F_3$ transition. Similarly the band at 701 nm is more likely to be the $^5D_0 \rightarrow {}^7F_4$ transition and the one observed in the 395 nm spectrum is also due to higher energy transitions. However as $^5D_0 \rightarrow {}^7F_0$, $^5D_0 \rightarrow {}^7F_1$, and $^5D_0 \rightarrow {}^7F_4$ do not change with excitation wavelength then these must originate from the $^5D_0$ lowest energy state.

There is also a small peak at around 530 nm related to the $^5D_1 \rightarrow {}^7F_1$ transition when excited at 395 nm. It is well known that some transitions originating from the $^5D_1$, $^5D_2$ and $^5D_3$ levels are commonly found in the emission spectra of some materials. However, these transitions are of much lower intensity than the $^5D_0 \rightarrow {}^7F_2$ transition (as in the case of the $^5D_1 \rightarrow {}^7F_1$ transition in this case) and this finding reinforces the effectiveness of radiationless decay taking place from higher energy levels to the $^5D_0$ level in this work [79].

3.6. Influence of Li+ in the host lattice

The incorporation of alkaline ions in some phosphor lattices can lead to many advantageous properties to both the host lattice and the activators ions present. It is known that Li^+ ions can be used as a flux to improve crystallinity and reduce internal reflections caused by rougher surfaces in thin-film. It is also well established that even in very small quantities, Li^+ coactivators frequently play an important role in the enhancement of the luminescent efficiency of phosphors, for instance in Gd_2O_3:Eu^{3+} thin-film phosphors doped by Li^+ ions the enhancement of luminescent intensity was 2.3 times [80]. When replacing/substituting for higher charged cations they can also create oxygen vacancies and possibly improve energy transfer properties (acting as sensitizers). In $Y_3Al_5O_{12}$ and Tm^{3+}-Li^+ co-activated $Y_3Al_5O_{12}$ in the visible nearly a 75% increase in luminescence was observed when Li^+ ions were added [81]. In addition, the enhancement effect of various doping ions has been associated with the effective ionic radius of the doping ions and the mismatch in electronegativity between doping ions and the other ions present in the lattice. The effect of co-doping M ions on enhanced photoluminescence of $GdTaO_4$:Eu^{3+} was investigated [82]. It was found that the improvement of luminescence intensity was closely related to the effective ionic radius of co-dopant and the mismatch in Pauling's electronegativity between co-dopant and Gd. The PL intensity of $GdTaO_4$:Eu^{3+} phosphor was improved by co-doping with Li^+,Mg^{2+},Zn^{2+}, or Al^{3+}whose radius is less than that of Gd^{3+}. In addition, the intensity increased with the electronegativity mismatch for co-doping with Li^+,Mg^{2+},Zn^{2+}, or Al^{3+} [82]. The Li^+ ion has the properties of manifesting small size, uniform size distribution and relatively regular spherical-like morphology. It is apparent that Li^+ cations favour high packing densities and enhance the brightness of the receiving phosphors [52,83].

The emission spectra of the Li^+ cation doped samples are presented in Fig. 14. The Eu^{3+} concentration was maintained at 1 mol% while Li^+ cation concentration was varied from 1 to 3 mol%. It is obvious that the position of the emission bands did not change due to doping with the additional Li^+ cations, but the co-doping increased the luminescence intensity (which optimised at 2 mol%) by around 50%. The enhancement of luminescence can be explained in terms of charge compensation phenomenon.

when Eu^{3+} substitutes Ag^+, the system acquires a net positive charge and this phenomenon avoids further substitution of Eu^{3+} due to an increase in the repulsive forces. This can result in an aggregation of Eu^{3+} ions on the surface of the material. In order to have a charge neutral condition, one Eu^{3+} ion can be substituted for three Ag^+ ions and consequently two Ag vacancies (V_{Ag}) would be created as explained in the discussion on the XRD studies above. These vacancies can reduce the overall intensity of the luminescence because they can act as defect sites that accept energy transfer from Eu^{3+} cations. By co-doping with the smaller Li^+ cations these effects are avoided/diminished and the non-radiative transition probability is lessened and the efficiency of radiative transitions is enhanced.

So as discussed in the XRD section, co-doping of Li^+ cations improves the crystallinity of samples reducing the concentration of defects and, consequently the probability of non-radiative transition. Another advantage of using Li_2CO_3 is that it also acts as a flux lowering the reaction temperature and enhances the incorporation of the Eu^{3+} activation agent into the host lattice, which in turn improve luminescence intensity [53].

The role of the O^{2-} vacancies in the emission process is complex localized on the surface of the material they may act as sensitizers and the energy transfer from the host to the Eu^{3+} ions by these sensitizers favours the mixing of the charge transfer states. Then, the luminous intensity is enhanced because the oscillator strength for the optical transition may be high because of the overlapping of the charge transfer states. However, co-doped Li^+ materials can affect the distribution of the O^{2-} vacancies as the Ag^+ substitution by Li^+ cations may alter their distribution and this may reduce luminescence intensity. So as the Li^+ concentration increases the O^{2-} vacancies may increase or redistribute disturbing the symmetry of the host lattice. Then, the photo-excited holes and electrons can be consumed by Ag^+ and O^{2-}, respectively. So excess Li^+ cations could have affects that hinder energy transfer from the host to the Eu^{3+}. Such defects avoid efficient radiative recombination and consequently, luminous intensity decreases. This process may account for the result observed for the sample with 3 mol% of Li^+ cations [53,60,61,84].

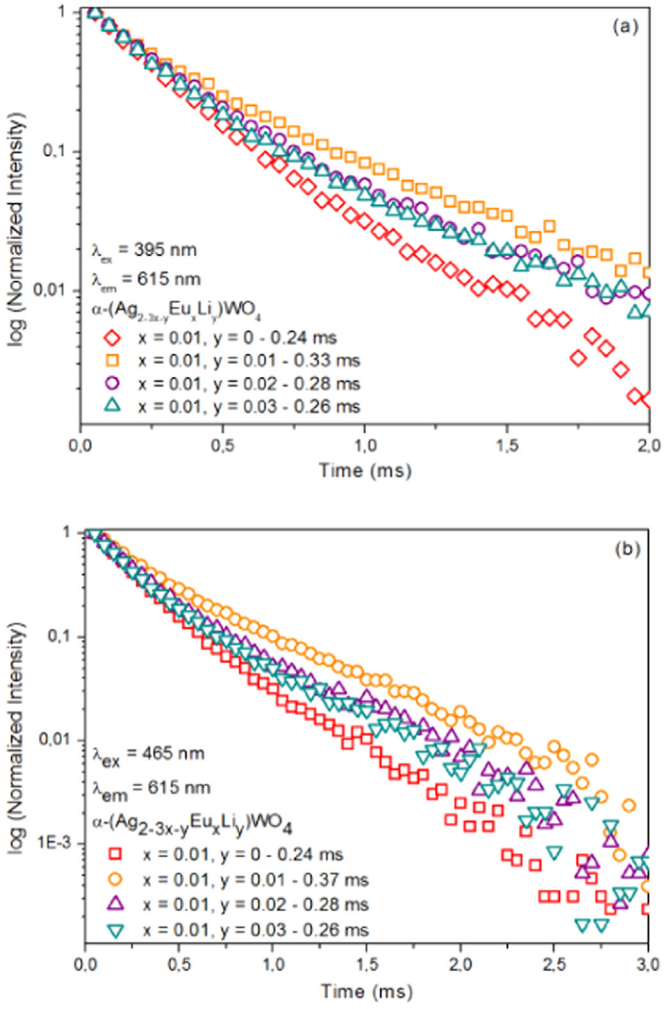

Fig. 15. PL decay curves of α-($Ag_{2-3\times-y}Eu_xLi_y$)WO_4 samples excited at (a) 395 and (b) 465 nm.

3.7. Photoluminescence decays

Generally, long emission lifetimes (of ms and more) are considered spectroscopic evidences for Eu^{3+} incorporation into nanoparticle lattice sites, in contrast to short lifetimes when the Eu^{3+} ions are located in a distorted environment [85]. In Fig. 15 (a) and (b) the PL decay curves are presented of the α-($Ag_{2-3\times-y}Eu_xLi_y$)WO_4 samples excited at 395 and 465 nm, respectively; while emission wavelength was monitored at 615 nm.

The PL decays were measured at room temperature and all curves could be well fitted to a first order exponential function represented in Eq. (3).

$$I(t) = I_0 e^{-t} \quad (3)$$

where I(t) is intensity at a given time t, I_0 is initial intensity and τ is a decay constant (lifetime). The lifetime values are all presented in

Fig. 15. All the curves are linear indicating only one depopulation mechanism is involved for the $^5D_0$ level. It is evidenced by the plot of the logarithm of the intensity against the time, which results in a linear relation. After 2 ms when excited at 395 nm and 3 ms when excited at 465 nm, the data points have low reliability because the signal/noise ratio became low, which may result in an "artificial" deviation of the linear behaviour. These are in accord with the occurrence of a single coordination environment for the Eu^{3+} ions and are in agreement with XRPD results discussed earlier.

The Li^+ co-doped samples present higher values compared to the Eu^{3+} -doped sample, indicating this sample has high energy vibrational oscillators around the Eu^{3+} ions. This may be due to the complex/more disorganized α-Ag_2WO_4 host lattice that contributes to the multi-phonon deactivation of the $^5D_0$ level. We have noted in discussion above that the Li^+ co-doped materials are more organised.

The excitation of the samples with the two different wavelengths viz; 395 nm ($^7F_0 \rightarrow {}^5L_6$ transition) and 465 nm ($^7F_0 \rightarrow {}^5D_2$ transition) results in almost identical decay constants (lifetimes) for each different Li^+ concentration. This indicates that radiationless decay from the higher energy levels ($^5L_6$ and $^5D_2$) to the $^5D_0$ level, is very fast and of the same order [79]. These phosphors manifest millisecond order lifetimes as expected for Eu^{3+} cations. Thus the main finding is that the photo-luminescent decay curves can be analysed in terms of one depopulation mechanism is in accord with the occurrence of a single coordination environment for the Eu^{3+} cations. This supports a single doping site for the Eu^{3+} cations in the α-$(Ag_{2-3\times-y}Eu_xLi_y)WO_4$ (where x = 0.01, y = 0.01–0.03 mol) samples.

Recently a red emitting phosphor based on Eu^{3+} has been successfully marketed for uses in applications in display and lighting. If the emission intensities of the phosphors studied herein could be improved they would be commercially useful as their main emission band is at 615 nm.

4. Conclusions

To sum up, nanometre-sized α-$(Ag_{2-3\times-y}Eu_xLi_y)WO_4$ phosphors were efficiently prepared by the co-precipitation method. The samples exhibited high luminescent efficiency as well as excellent chemical stability. Li^+ cations improved the crystallinity of samples reducing the concentration of defects and, consequently the probability of non-radiative transition, thereby improving the luminescence. The emission colour of the resulting phosphors was in the red region and the most intense and pure one was for 1 mol% Eu^{3+} and 2 mol% Li^+. Although silver tungstate has different sites coordination, the results attest for the occurrence of two coordination sites of low symmetry for the Eu^{3+} ions. These results conclude that although the main emission wavelength (615 nm) of these phosphors is suitable as a red component for white LEDs in solid state lighting applications this will only be possible if their emission brightness can be further improved. However these phosphors may have uses for LEDs in backlights for displays in the longer term.

Acknowledgements

[a]We are grateful to the EPSRC and Technology Strategy Board (TSB) for funding the PURPOSE (TP11/MFE/6/1/AA129F; EP-SRC TS/G000271/1) and CONVERTED (JeS no. TS/1003053/1), PRISM (EP/N508974/1) and FAB3D programs. We are finally grateful to the TSB for funding the CONVERT program.

[b]The authors appreciate the support of FAPESP (São Paulo Research Foundation, Grant#2013/07296-2, Grant#2013/23995-8 and Grant#2015/13669-1). They also wish to thank Rorivaldo Camargo for technical and scientific contributions.

References

[1] J. Silver, R. Withnall, A. Kitai (Ed.), Luminescent Materials and Applications, Wiley, England, 2008, pp. 75–109.
[2] I.M. Pinatti, T.G. Ireland, G.R. Fern, I.L.V. Rosa, J. Silver, J. Mater. Sci. Electron. 28 (2016) 7029–7035.
[3] J. Wang, Z.-J. Zhang, J.-T. Zhao, H.-H. Chen, X.-X. Yang, Y. Tao, Y. Huang, J. Mater. Chem. 20 (2010) 10894.
[4] J. Lin, J. Yang, J. Gao, Q. Wang, Polyhedron 113 (2016) 102–108.
[5] W.J. Zhang, W.L. Feng, Y.M. Nie, Optik 126 (2015) 1341–1343.
[6] S.K. Gupta, K. Sudarshan, P.S. Ghosh, K. Sanyal, A.P. Srivastava, A. Arya, P.K. Pujari, R.M. Kadam, RSC Adv. 6 (2016) 3792–3805.
[7] B.P. Maheshwary, Singh, R.A. Singh, Spectrochim. Acta A 152 (2016) 199–207.
[8] T.-C. Chien, J.-C. Yang, C.-S. Hwang, M. Yoshimura, J. Alloy. Compd. 676 (2016) 286–291.
[9] K.K. Rasu, D. Balaji, S.M. Babu, J. Lumin. 170 (2016) 547–555.
[10] K.K. Rasu, D. Balaji, S.M. Babu, J. Lumin. 170 (2016) 825–834.
[11] T. Liu, Q. Meng, W. Sun, J. Lumin. 170 (2016) 219–225.
[12] Y. Wang, J. Tang, X. Huang, L. Jiang, J. Rare Earths 34 (2016) 118–124.
[13] W. Zhang, C. Yuan, R. Hua, T. Liu, K. Song, J. Yu, D. Tang, Y. Gao, B. Chen, J. Nanosci. Nanotechnol. 16 (2016) 822–827.
[14] K. Song, G.-M. Li, J. Mater. Sci. Electron. 27 (2015) 1227–1231.
[15] Y. Zhai, M. Wang, Q. Zhao, J. Yu, X. Li, J. Lumin. 172 (2016) 161–167.
[16] X. Qiao, S. Qi, Y. Lu, Y. Pu, Y. Huang, X. Wang, J. Alloy.Compd. 656 (20160 189-195.
[17] X. Feng, W. Feng, M. Xia, K. Wang, H. Liu, D. Deng, X. Qin, W. Yao, W. Zhu, RSC Adv. 6 (20160 14826-14831.
[18] H. Zhu, M. Fang, Z. Huang, Y.G. Liu, K. Chen, X. Min, Y. Mao, M. Wang, J. Lumin. 172 (2016) 180–184.
[19] C. Chen, C. Li, Z. Shi, Adv. Sci. 3 (2016) 1600029.
[20] A.M. Kaczmarek, R. Van Deun, Chem. Soc. Rev. 42 (2013) 8835–8848.
[21] A.K. Vishwakarma, K. Jha, M. Jayasimhadri, A.S. Rao, K. Jang, B. Sivaiah, D. Haranath, J. Alloy. Compd. 622 (2015) 97–101.
[22] Y. Zhang, H. Jiao, Y. Du, J. Lumin. 131 (2011) 861–865.
[23] E. Biémont, P. Quinet, Phys. Scr. T105 (2003) 38–54.
[24] C.A. Kodaira, H.F. Brito, O.L. Malta, O.A. Serra, J. Lumin. 101 (2003) 11–21.
[25] Y. Wang, Y. Qu, K. Pan, G. Wang, Y. Li, ChemComm 52 (2016) 11124–11126.
[26] V. Muhr, M. Buchner, T. Hirsch, D.J. Jovanović, S.D. Dolić, M.D. Dramićanin, O.S. Wolfbeis, Sens. Actuators B-Chem. 241 (2017) 349–356.
[27] C.A. Kodaira, H.F. Brito, M.C.F.C. Felinto, J. Solid State Chem. 171 (2003) 401–407.
[28] S. Gai, C. Li, P. Yang, J. Lin, Chem. Rev. 114 (2014) 2343–2389.
[29] P.M. Skarstad, S. Geller, Mater. Res. Bull. 10 (1975) 791–799.
[30] L.S. Cavalcante, M.A. Almeida, W. Avansi Jr., R.L. Tranquilin, E. Longo, N.C. Batista, V.R. Mastelaro, M.S. Li, Inorg. Chem. 51 (2012) 10675–10687.
[31] J. Andres, L. Gracia, P. Gonzalez-Navarrete, V.M. Longo, W. Avansi Jr., D.P. Volanti, M.M. Ferrer, P.S. Lemos, F.A. La Porta, A.C. Hernandes, E. Longo, Sci. Rep. 4 (2014) 5391.
[32] I.M. Pinatti, I.C. Nogueira, W.S. Pereira, P.F. Pereira, R.F. Goncalves, J.A. Varela, E. Longo, I.L. Rosa, Dalton Trans. 44 (2015) 17673–17685.
[33] Q.-W. Song, B. Yu, X.-D. Li, R. Ma, Z.-F. Diao, R.-G. Li, W. Li, L.-N. He, Green Chem. 16 (2014) 1633.
[34] C.-X. Guo, B. Yu, J.-N. Xie, L.-N. He, Green Chem. 17 (2015) 474–479.
[35] L. Cheng, Q. Shao, M. Shao, X. Wei, Z. Wu, J. Phys. Chem. C 113 (2009) 1764–1768.
[36] R. Zhang, H. Cui, X. Yang, H. Liu, H. Tang, Y. Li, Micro Nano Lett. 7 (2012) 1285–1288.
[37] X. Liu, J. Hu, J. Li, Y. Hu, Y. Shao, H. Yang, G. Tong, H. Qian, Mater. Lett. 91 (2013) 129–132.
[38] H. Chen, Y. Xu, Appl. Surf. Sci. 319 (2014) 319–323.
[39] J. Tang, J. Ye, J. Mater. Chem. 15 (2005) 4246–4251.
[40] X. Wang, C. Fu, P. Wang, H. Yu, J. Yu, Nanotechnology 24 (2013) 165602.
[41] Z. Lin, J. Li, Z. Zheng, J. Yan, P. Liu, C. Wang, G. Yang, ACS Nano 9 (2015) 7256–7265.
[42] D. Stone, J. Liu, D.P. Singh, C. Muratore, A.A. Voevodin, S. Mishra, C. Rebholz, Q. Ge, S.M. Aouadi, Scr. Mater. 62 (2010) 735–738.
[43] L. Pan, L. Li, Y. Chen, J. Sol-Gel Sci. Technol. 66 (2013) 330–336.
[44] L.F. da Silva, A.C. Catto, W. Avansi Jr., L.S. Cavalcante, J. Andres, K. Aguir, V.R. Mastelaro, E. Longo, Nanoscale 6 (2014) 4058–4062.
[45] L.F. da Silva, A.C. Catto, W. Avansi, L.S. Cavalcante, V.R. Mastelaro, J. Andrés, K. Aguir, E. Longo, J. Alloy. Compd. 683 (2016) 186–190.
[46] A. Sreedevi, K.P. Priyanka, S.R. Mary, E.M. Mohammed, T. Varghese, Adv. Sci. Eng. Med. 7 (2015) 498–505.
[47] Q. Wang, X. Guo, W. Wu, S. Liu, Adv. Mater. Res. **284**-286 (2011) 1321–1325.
[48] D.P. Dutta, A. Singh, A. Ballal, A.K. Tyagi, Eur. J. Inorg. Chem. 2014 (2014) 5724–5732.
[49] V.M. Longo, C.C. De Foggi, M.M. Ferrer, A.F. Gouveia, R.S. Andre, W. Avansi, C.E. Vergani, A.L. Machado, J. Andres, L.S. Cavalcante, A.C. Hernandes, E. Longo, J. Phys. Chem. A 118 (2014) 5769–5778.
[50] A. Sreedevi, K.P. Priyanka, K.K. Babitha, S. Ganesh, T. Varghese, Micron 88 (2016) 1–6.
[51] C. Litterscheid, S. Krüger, M. Euler, A. Dreizler, C. Wickleder, B. Albert, J. Mater. Chem. C 4 (2016) 596–602.
[52] Y. Ma, W. Ran, W. Li, C. Ren, H. Jiang, J. Shi, Luminescence 31 (2016) 665–670.
[53] Y. Zhai, Y. Han, W. Zhang, Y. Yin, X. Zhao, J. Wang, X. Liu, J. Alloy. Compd. 688 (2016) 241–247.
[54] F. Lei, B. Yan, H.H. Chen, J.T. Zhao, J. Am. Ceram. Soc. 92 (2009) 1262–1267.
[55] A. Sreedevi, K.P. Priyanka, K.K. Babitha, N. Aloysius Sabu, T.S. Anu, T. Varghese, Indian J. Phys. 89 (2015) 889–897.
[56] H.P. Barbosa, J. Kai, I.G.N. Silva, L.C.V. Rodrigues, M.C.F.C. Felinto, J. Hölsä, O.L. Malta, H.F. Brito, J. Lumin. 170 (2016) 736–742.

[57] L. Vegard, Z. Phys. 5 (1921) 17–26.
[58] R.D. Shannon, Acta Cryst. A32 (1976) 751–767.
[59] J. Silver, R. Withnall, Chem. Rev. 104 (2004) 2833–2855.
[60] D.K. Singh, P.K. Baitha, J. Manam, Appl. Phys. A 122 (2016) 668.
[61] B.H. Min, J.C. Lee, K.Y. Jung, D.S. Kim, B.-K. Choi, W.-J. Kang, RSC Adv. 6 (2016) 81203–81210.
[62] K. Momma, F. Izumi, J. Appl. Crystallogr. 44 (2011) 1272–1276.
[63] F. Cheng, Z. Xia, M.S. Molokeev, X. Jing, Dalton Trans. 44 (2015) 18078–18089.
[64] R. Withnall, M.I. Martinez-Rubio, G.R. Fern, T.G. Ireland, J. Silver, J. Opt. A Pure Appl. Opt. 5 (2003) S81–S85.
[65] A. Turkovic, D.L. Fox, J.F. Scott, Mat. Res. Bull. 1Z (1977) 189–196.
[66] H.-H. Xi, D. Zhou, H.-D. Xie, B. He, Q.-P. Wang, N. Alford, J. Am. Ceram. Soc. 98 (2015) 587–593.
[67] T. Linda Francis, P. Prabhakar Rao, S.K. Mahesh, T.S. Sreena, S. Parvathi Babu, Opt. Mater. 52 (2016) 134–143.
[68] D. Balaji, K. Kavirasu, A. Durairajan, S. Moorthy Babu, J. Alloy. Compd. 637 (2015) 350–360.
[69] J. Silver, M.I. Martinez-Rubio, T.G. Ireland, G.R. Fern, R. Withnall, J. Phys. Chem. B 105 (2001) 9107–9112.
[70] W. You, Z. Xiao, F. Lai, X. Ye, Q. Zhang, H. Jiang, C. Wang, J. Liao, X. Liu, S. Zhong, J. Mater. Sci. 51 (2016) 5403–5411.
[71] S. Shi, X. Liu, J. Gao, J. Zhou, Spectrochim. Acta A 69 (2008) 396–399.
[72] J. Huang, J. Xu, H. Luo, X. Yu, Y. Li, Inorg. Chem. 50 (2011) 11487–11492.
[73] P.F.S. Pereira, A.P. de Moura, I.C. Nogueira, M.V.S. Lima, E. Longo, P.C. de Sousa Filho, O.A. Serra, E.J. Nassar, I.L.V. Rosa, J. Alloy. Compd. 526 (2012) 11–21.
[74] X. Wang, B. Liu, Y. Yang, Opt. Laser Technol. 58 (2014) 84–88.
[75] P.S. Dutta, A. Khanna, ECS J. Solid State Sci. Technol. 2 (2012) R3153–R3167.
[76] S. Balaji, P. Abdul Azeem, R.R. Reddy, Phys. B Condens. Matter 394 (2007) 62–68.
[77] R.R. Pereira, F.T. Aquino, A. Ferrier, P. Goldner, R.R. Gonçalves, J. Lumin. 170 (9) (2016) 707–717.
[78] K. Gayatri Sharma, N. Shanta Singh, Y. Rangeela Devi, N. Rajmuhon Singh, S. Dorendrajit Singh, J. Alloy. Compd. 556 (2013) 94–101.
[79] M. Janulevicius, P. Marmokas, M. Misevicius, J. Grigorjevaite, L. Mikoliunaite, S. Sakirzanovas, A. Katelnikovas, Sci. Rep. 6 (2016) 26098.
[80] S.-S. Yi, J.S. Bae, K.S. Shim, J.H. Jeong, J.-C. Park, P.H. Holloway, Appl. Phys. Lett. 84 (2004) 353–355.
[81] O.A. Lopez, J. McKittrick, L.E. Shea, J. Lumin. 71 (1997) 1–11.
[82] X. Liu, K. Han, M. Gu, L. Xiao, C. Ni, S. Huang, B. Liu, Solid State Commun. 142 (2007) 680–684.
[83] B. Liu, M. Gu, X. Liu, K. Han, S. Huang, C. Ni, G. Zhang, Z. Qi, Appl. Phys. Lett. 94 (2009) 061906.
[84] C. Liu, J. Liu, J. Phys. Chem. B 110 (2006) 20277–20281.
[85] V.I. Parvulescu, C. Tiseanu, Catal. Today 253 (2015) 33–39.